www.czasopisma.pan.pl PAN POLSKA AKADEMIA NAUK www.journals.pan.pl

Arch. Metall. Mater. **67** (2022), 3, 931-938

DOI: https://doi.org/10.24425/amm.2022.139685

ERKAN ÜSTÜN[1], EMIN ÇADIRLI[2*]

EFFECT OF GROWTH RATE ON COARSENING OF SECONDARY DENDRITE ARM SPACINGS IN DIRECTIONALLY SOLIDIFIED OF Al-8.8La-1.2Ni TERNARY ALLOY

One of the most important factors directly affecting microstructure and mechanical properties in directional solidification process is secondary dendrite arm spacing (SDAS). It is very important to measure the SDAS and examine the factors that may affect them. To investigate the effect of growth rate on the SDAS, the alloy specimens were directional solidified upward with different growth rates (V = 8.3-83.0 μm/s) at a constant temperature gradient (G = 4 K/mm) in a Bridgman-type growth apparatus. After the specimens are directionally solidified, they were exposed to metallographic processes in order to observe the dendritic solidification structure on the longitudinal section of the specimens. Coarsen secondary dendrite arm spacings (λ_{2C}) were measured excluding the first arms near the tip of the dendrite. Local solidification times (t_f) were calculated by ratio of spacings to growth rates. It was determined that the t_f values decreased with increasing V values. The relationships between t_f and λ_{2C} were defined by means of the binary regression analysis. Exponent values of t_f were obtained as 0.37, 0.43, 0.46 and 0.47 according to increasing V values, respectively. These exponent values are close to the exponent value (0.33) predicted by the Rappaz-Boettinger theoretical model and good agreement with the exponent values (0.33-0.50) obtained by other experimental studies.

Keywords: Directional solidification; Al-La-Ni ternary alloys; coarsening; secondary dendrite arm spacing

1. Introduction

The main factor that determines the mechanical properties of the materials is the microstructure of the material. One of the most important factors directly affecting the microstructure is the secondary dendrite arm spacing (SDAS), which depends on the growth rate during solidification. There are many studies in the literature on this subject [1-10]. In the theoretical models proposed in these studies, it was stated that SDAS (λ_2) is proportional to a power of local solidification time (t_f) [11-17]. During solidification, the secondary arms tend to increase their spacing owing to different facts, namely: re-melting of small secondary dendrites, melting of dendrite roots or coalescence between dendrites [4-8]. The first researchers in detecting this feature were Kattamis et al. [13] and Flemings et al. [14] and nowadays it is believed to arise from surface stresses at the liquid-solid interface. Dendritic array demonstrates an obvious branching of primary and secondary dendritic arms, in which the scale of λ_2 is a very common microstructure parameter used as an indicative of casting quality [17].

Aluminium-based alloys are common preferred in practice due to their low density and high strength [18-21]. Al-La-Ni ternary alloys are well known for their well glass forming skill by fast quenching from the liquid state [18] and for their skill for hydrogen storage within the solid state [19]. Several investigations have been carried out on selected compositions in order to study hydrogen storage, crystal structures, some mechanic and thermal properties of Al-La-Ni alloys [20,21].These alloys have been found to exhibit a particularly beneficial combination of high strength and low density, making them promising candidates for technological applications.

However, very limited information is available in the literature regarding the industrially important ternary Al-La-Ni alloy. In this sense, the main purpose of this paper is to investigate the effects of different growth rates (V = 8.3-83.0 mm/s) on dendritic microstructure of directionally solidified Al-8.8La-1.2Ni (wt.%) alloy at a constant temperature gradient (G = 4 K/mm) in a Bridgman-type growth apparatus. In addition, it is to compare the experimental SDAS values, which are known to be quite effective on mechanical properties, with the SDAS values calculated from the Rappaz-Boettinger theoretical model [22].

[1] NIĞDE ÖMER HALISDEMIR UNIVERSITY, INSTITUTE OF SCIENCE, DEPARTMENT OF PHYSICS, NIĞDE, TURKEY
[2] NIĞDE ÖMER HALISDEMIR UNIVERSITY, FACULTY OF ARTS AND SCIENCES, DEPARTMENT OF PHYSICS, NIĞDE, TURKEY
* Corresponding author: ecadirli@gmail.com

The model proposed by Kattamis et al. [13] for SDAS calculation of binary alloys has been expanded for multicomponent alloys by Rappaz and Boettinger (R-B model) [22]. The general expression is given as follows;

$$\lambda_2 = 5.5\left(\frac{-\Gamma}{\Sigma_{j=1}^{n} m_j\left(1-k_j\right)\left(c_{f,j}-c_{o,j}\right)/D_j \ln\left[\frac{\sum_{j=1}^{n} m_j\left(1-k_j\right)c_{f,j}/D_j}{\sum_{j=1}^{n} m_j\left(1-k_j\right)c_{o,j}/D_j}\right]}\right)^{\frac{1}{3}} (t_f)^{\frac{1}{3}} \quad (1)$$

where t_f, is the local solidification time, Γ is the Gibbs-Thomson coeffcient, mj is the liquidus slope, $c_{f,j}$ is the final liquid composition at the dendrite root of the component j (generally assumed to be a eutectic composition), $c_{o,j}$ is the nominal composition of the alloy, D_j is the diffusion coefficient in the liquid, n is the maximum number of solute elements (j = 1, n) and k_j is the redistribution coefficient. The subscript j represents each alloying element, and the sum encompasses all the solute elements of the multicomponent alloy.

Some researchers [23,24] examined the effects of liquid flow on λ_2 for different alloys and showed that the exponent value of the local solidification time (t_f) deviated from 1/3 value, close to 1/2. Easton et al. [25] compared the experimental λ_2 values of six different multi-component Al alloys with the values calculated from the Rappaz and Boettinger [22] model. These researchers reported that the values overlapped by up to 70%. During the coarsening, the dendrites minimize the free energy of the solid-liquid system and which over time cause the solid-liquid interface area [3] to decrease are subjected to diffusion mass transfer [1] controlled by the local interface curvature [2]. This situation leads to significant morphological changes in the dendritic microstructure, including the re-melting of small branches [4,5], multiplication [6] and coalescence [7,8]. Coarsening is particularly important after dendrite coherency, when free growth stops and the feeding shifts from mass to interdendritic [9]. Then, the eutectic reaction takes place in the interdendritic regions [10] and solidification is completed.

The coarsening mechanisms have been proposed either based on the observations of solidification of transparent materials (case I) or observations of the microstructures of alloys after solidification were interrupted by quenching (case II) [12,13]. There are hardly any studies on how growth rate affects the exponent of t_f for the studied alloy.

2. Experimental Method

2.1. Specimen preparation, solidification and metallographic process

Directional solidification experiments were carried out with Al-8.8La-1.2Ni (wt %) ternary alloy, prepared from the weighing of its high purity Al metal and La-12wt.%Ni alloy rod (*alloys attributed in this study were given by weight percent unless otherwise stated*). During the specimen preparation, metal and master La-12Ni alloy with a purity of more than 99.9% were used to minimize impurities that may occur on the interface and structural defects caused by this situation. Vacuum melting furnace and casting furnace were used in the melting and pouring processes, respectively. The vacuum melting furnace provides a process temperature of 1100°C under an atmosphere of approximately 10^{-3} torr. Using this furnace, up to approximately 2 kg of material can be melted at one time. First, aluminium was melted in a graphite crucible placed inside the vacuum melting furnace, and then La-12Ni master alloy was added into this Al melt and completely melted. For the studied alloy, the starting (T_{onset}) and ending (T_{peak}) temperatures of the melting were determined as 914 and 939 K, respectively. During this melting process, the alloy was mixed several times to make it homogeneous. Then this homogeneous melt alloy poured into the graphite crucibles (6.35 mm OD, 4 mm ID, and 250 mm in length) placed inside the casting furnace without any air bubbles. In this way, a large number of alloy specimens with the same composition were prepared. Each of these prepared specimens was placed inside the Bridgman-type growth apparatus [26] for controlled directional solidification. Then each specimen was drawn from the hot zone to the cold zone with different growth rates (8.3-83.0 μm/s) via synchronous motors at a constant temperature gradient (4 K/mm). These specimens were quenched in water at 10°C after solidifying about 10 cm. To obtain the image analysis and microstructure of the specimens, each specimen was subjected to metallographic processes such as grinding, polishing, and etching with a suitable reagent, respectively. Dendritic microstructures of the specimens were revealed after metallographic processes. The dendritic microstructures of specimens were photographed with Olympus BX-51 optical microscope.

2.2. Measurement of the G and V

During the solidification of the specimen in the Bridgman-type apparatus, the temperature gradient and growth rates in the specimen were determined by three K-type thermocouples that previously placed in the specimen at 5 mm spacing. The temperature gradient ($G = \Delta T/\Delta X$) of the liquid phase and the growth rate of the solid-liquid interface ($V = \Delta X/\Delta t$) were calculated by determining the values of ΔT, ΔX, and Δt for each specimen. Where ΔT is the temperature difference between the liquid and solid-liquid interface, ΔX is the distance between the thermocouples (5 mm), and Δt is the time required for the solid-liquid interface to travel the distance between the two thermocouples.

The growth rates are provided by four synchronous motors with different rpm (1, 2, 5 and 10 rpm). While 1 rpm provides a growth rate of 8.3 μm/s, 10 rpm provides a growth rate of 83 mm/s. Bridgman-type apparatus provided cooling rate in the range of 0.033-0.33 K/s depending on the solidification parameters (G, V) in this study. Besides, a cooling rate of 25 K/s is reached in industrial scale Bridgman-type furnaces depending on the solidification parameters [27].

2.3. Measurements of λ_{2C} and t_f in the process of coarsening

With the Adobe Photoshop CS3 program, the coarsen secondary dendrite arm spacings (λ_{2C}) on the longitudinal section images of the specimen were measured as a function of time by excluding the first few arms close to the dendrite tip. Because it is known that there is no coarsening in the region near the tip of the dendrite. By dividing these measurements into the growth rate, local solidification times (t_f) were calculated for each SDAS (Fig. 1a). As can be seen from Fig. 1a, the fine arms close to the dendrite tip and the coarse arms near the root are shown as A and B, respectively. Typical images of growth morphologies (dendritic form) of directionally solidified Al-8.8La-1.2Ni alloy at the lowest and highest growth rates are shown in Figs. (1b, c). These measurement processes were repeated for the statistical reliability of the results for about 30-35 dendrite trunks at each growth rate.

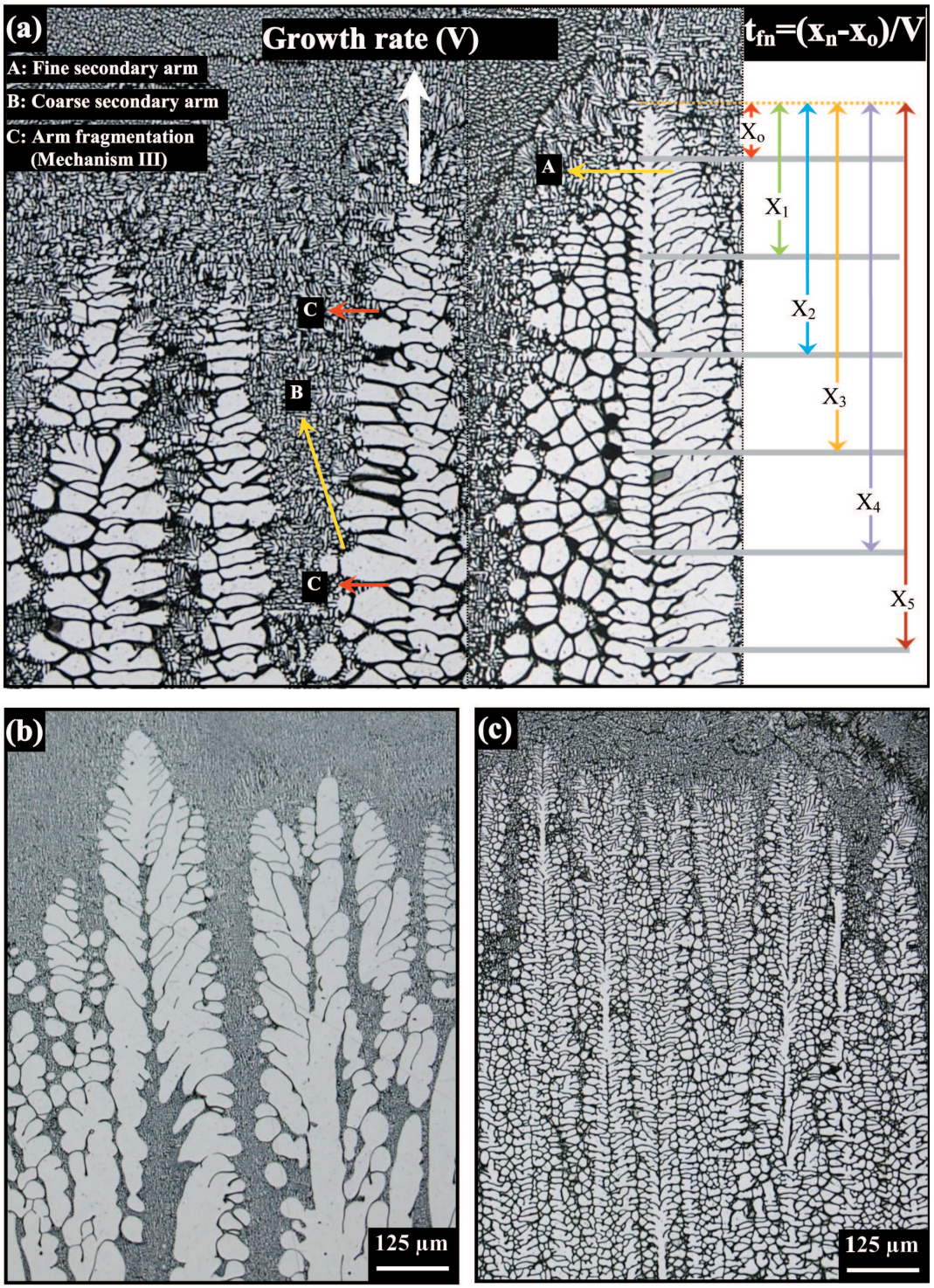

Fig. 1. Typical optical micrographs of the directionally solidified Al-8.8La-1.2Ni alloy at a constant G (4 K/mm); (a) measurements of λ_2 and t_f, (b) V = 8.3 µm/s, (c) V = 83.0 µm/s

3. Results and Discussion

3.1. Coarsening mechanisms

During coarsening, the larger arms grow, while the smaller ones shrink or re-melting by transport of material from the smaller arms to the larger ones. To explain this situation (coarsening of the SDAS), four coarsening mechanisms, i.e. radial melting (Mechanism I), axial melting (Mechanism II), arm fragmentation (Mechanism III), and coalescence (Mechanism IV) were proposed [11,13,28,29] as shown in Fig. 2. These mechanisms involve mass transport driven by the Gibbs-Thomson effect (also known as the capillary force). That is, the difference in local curvatures at the liquid-solid interface causes the surfaces with high curvature to melt due to the depression in liquidus temperature, and those surfaces with low curvature tend to grow coarser by diffusion. Depending on the growth kinetics of the secondary arms, it can be said to depend on the competitive growth of the arms during solidification. During this competitive growth, one or more of previously mentioned coarsening mechanisms are considered to have a dominant effect on this process. The phenomenon observed in this study was determined to be more compatible with mechanism III (arm fragmentation). In the mechanism III a neck forms at the root of an arm [28]. With increasing time (1-2 minutes) further re-melting occurs at the neck with freezing at areas of lower curvature until the arm becomes disconnected from the dendrite trunk and gradually spheroidized. The final step of Mechanism III is shown with C in Fig. 1a.

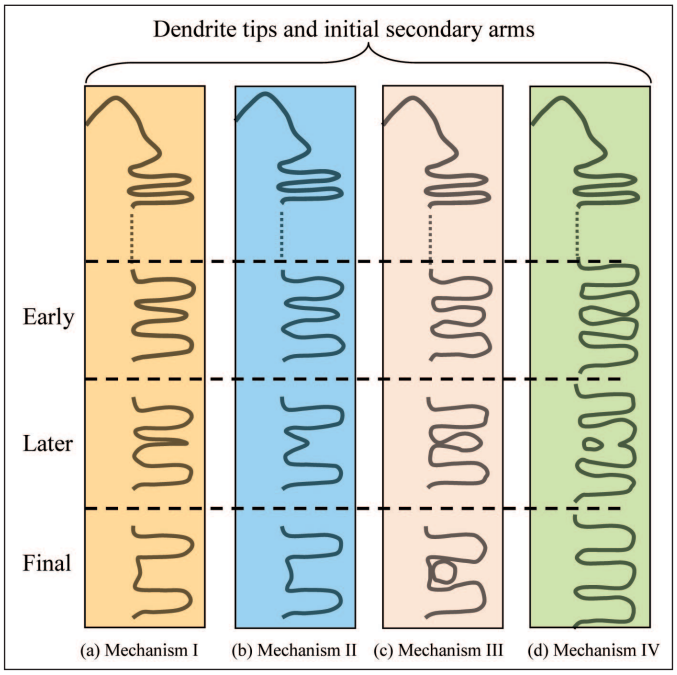

Fig. 2. Four mechanisms for isothermal dendrite coarsening; (a) radial re-melting, (b) axial re-melting, (c) arm fragmentation, (d) coalescence of two dendrite arms

3.2. Effect of growth rate on the λ_{2C}

From the micrographs in Figs. (1b, c) and as can be seen from the values obtained by us in Fig. 3, it was seen that the SDAS, which became coarse with increasing solidification rate (V), decreased. Possible effects of different growth rates on coarsen secondary arm spacing (λ_{2C}) were investigated. In Fig. 3, the experimental values obtained by us are compared with the experimental values obtained by some researchers [30-34] and the values predicted from the Rappaz-Boettinger model [22]. From the micrographs in Figs. (1b, c) and as can be seen from the experimental values obtained by us in Fig. 3, it was seen that the SDAS, which became coarse with increasing growth rate (V), decreased. Therefore, local solidification time (t_f) values decreased with increasing V. In a study by Chen and Kattamis [33], a similar behavior was reported for the Al-3.75Cu-1.5Mn alloy using almost the same growth rates. The relationships between these parameters were found using linear regression analysis. The relationships between λ_{2C} and local solidification time (t_f) for each V (8.3-83.0 mm/s) are given in TABLE 1. Rappaz-Boettinger model (R-B model) is represented in Fig. 3

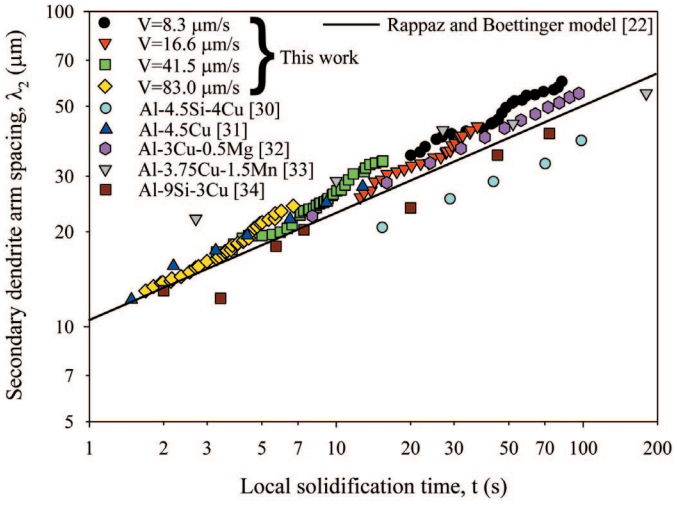

Fig. 3. Variation of secondary dendrite arm spacing as a function of lacal solidification time

TABLE 1

The experimental relationships between SDAS (λ_{2C}) and local solidification time (t_f)

Motors	G (K/mm)	V (μm/s)	Relationships	Constants (k)	Correlation coefficients (r)
1 rpm	4	8.3	$\lambda_{2C} = k_1 t_f^{0.37}$	$k_1 = 11.38$ (μm s$^{-0.37}$)	$r_1 = 0.984$
2 rpm	4	16.6	$\lambda_{2C} = k_2 t_f^{0.43}$	$k_2 = 8.97$ (μm s$^{-0.43}$)	$r_1 = 0.984$
5 rpm	4	41.5	$\lambda_{2C} = k_3 t_f^{0.46}$	$k_3 = 9.41$ (μm s$^{-0.46}$)	$r_1 = 0.983$
10 rpm	4	83.0	$\lambda_{2C} = k_4 t_f^{0.47}$	$k_4 = 9.77$ (μm s$^{-0.47}$)	$r_1 = 0.990$

by the dashed line. Some physical constants required for the studied alloy for the R-B model (Eq. (1)) are given in TABLE 2. Substituting these physical constants into Eq. (1) for the studied alloy, the λ_{2C} values predicted by the R-B model were obtained. The λ_{2C} values predicted by the R-B model [22] for the studied alloy nearly overlap with the experimental λ_{2C} values obtained by us. As can be seen from TABLE 1, the exponential values of t_f were obtained as 0.37, 0.43, 0.46 and 0.47 according to increasing V values (8.3-83.0 μm/s).

TABLE 2

Physical constants used in calculations for the Rappaz-Boettinger model [22]

	Al-Ni [35]	**Al-La [36]**
G (K m)	7.4×10^{-7}	3.5×10^{-8}
$m\alpha$ (K/wt.%)	–3.12	–10
k	0.00789	0.00514
C_E (wt.%)	5.7	19.6
C_o (wt.%)	1.2	8.8
D_L (m^2/s)	1.34×10^{-9}	1.15×10^{-9}

The experimental relationships compiled from some previous studies [26,30-34,37-44] are given in TABLE 3. In this Table, the solidification parameters used by various researchers [31,32,40-44] are both lower and higher the solidification parameter ranges we use, such as V (8.3-83 μm/s), and cooling rate (0.033-0.33 K/s). In TABLE 3, the experimental relationships obtained under different solidification conditions (G, V or cooling rate) for various alloys are shown. Also TABLE 3 has been contains some as cast [30] and numerical simulation studies [34]. The exponent values (0.37, 0.43, 0.46 and 0.47) obtained in this work are good agreement with the values of 0.47, 0.40, 0.33, 0.37, 0.34 and 0.47 reported by Tiryakioğlu [30] for Al-4.5Si-1Cu and Al-4.5Si-4Cu, by Ferreira et al. [31] for Al-4.5Cu, by Ferreira et al. [32] for Al-3Cu-0.5Mg, by Donadoni et al. [34] for Al-9Si-3Cu and by Matache et al. [37] for CMSX-4, respectively. Besides, the exponent values of 0.23, 0.27, 0.26, and 0.26 reported by Chen and Kattamis [33] for Al-3.75Cu-1.5Mn, by Ronto and Roosz [40] for Al-3.7Cu-0.47Si and Al-3.85Cu-0.95Si, and by Ronto and Roosz [41] for Al-1.24Mg-0.45Si are smaller than both the our experimental exponent values and the theoretical value suggested by the Rappaz-Boettinger [22] theoretical model, respectively. In TABLE 3, the exponent values of t_f are in the range of 0.23-0.54, while the k constants are in the range of 3.16-101.3. In this study, the values of the experimental exponent (0.36-0.47) and k constants (8.97-11.38) fall within these ranges. While exponent values show the degree of dependence on local solidification time (t_f), experimental k values vary depending

TABLE 3

The experimental relationships and constants between λ_{2C} and t_f under certain solidification conditions (G, V and cooling rate) compiled from previous works

Alloys	***G*** **(K/mm)**	***V*** **(mm/s)**	**Cooling rate (K/s)**	**Relationships**	**Constants (*k*)**
Al-0.2Si-0.3Fe [25]	—	—	0.3-15	$\lambda_{2C}=k_1t_f^{0.40}$	$k_1=91.30$ (μm $s^{-0.40}$)
Al-0.5Si-0.3Mg [25]	—	—	0.3-15	$\lambda_{2C}=k_2t_f^{0.50}$	$k_2=101.30$ (μm $s^{-0.50}$)
Al-4.5Si-1Cu [30]***	—	—	—	$\lambda_{2C}=k_3t_f^{0.47}$	$k_3=3.16$ (μm $s^{-0.47}$)*
Al-4.5Si-4Cu [30]***	—	—	—	$\lambda_{2C}=k_4t_f^{0.40}$	$k_4=4.74$ (μm $s^{-0.40}$)*
Al-4.5Cu [31]	—	—	5-45	$\lambda_{2C}=k_5t_f^{0.33}$	$k_5=12.10$ (μm $s^{-0.33}$)
Al-3Cu-0.5Mg [32]	1-16 (**)	0.6-1.5 (**)	0.6-24	$\lambda_{2C}=k_6t_f^{0.37}$	$k_6=10.09$ (μm $s^{-0.37}$)
Al-3.75Cu-1.5Mn [33]	6.8	0.002-0.083	0.14-0.56	$\lambda_{2C}=k_7t_f^{0.23}$	$k_7=17.98$ (μm $s^{-0.23}$)*
Al-9Si-3Cu [34]	Data from the Thermo-Calc software			$\lambda_{2C}=k_8t_f^{0.34}$	$k_8=9.53$ (μm $s^{-0.34}$)*
CMSX-4 super alloy [37]	3	3	9	$\lambda_{2C}=k_9t_f^{0.47}$	$k_9=6.70$ (μm $s^{-0.47}$)
CMSX-4 super alloy [38]	3	0.05	0.15	$\lambda_{2C}=k_{10}t_f^{0.54}$	$k_{10}=4.58$ (μm $s^{-0.54}$)
Al-7Si-0.5Mg [39]	0.3-1.9	0.037-0.256	0.01-0.48	$\lambda_{2C}=k_{11}t_f^{0.30}$	$k_{11}=10.70$ (μm $s^{-0.30}$)
Al-3.7Cu-0.47Si [40]	—	—	0.08-0.29	$\lambda_{2C}=k_{12}t_f^{0.27}$	$k_{12}=14.87$ (μm $s^{-0.27}$)
Al-3.85Cu-0.95Si [40]	—	—	0.08-0.29	$\lambda_{2C}=k_{13}t_f^{0.26}$	$k_{13}=16.39$ (μm $s^{-0.26}$)
Al-2.41Cu-0.75Si [40]	—	—	0.08-0.29	$\lambda_{2C}=k_{14}t_f^{0.31}$	$k_{14}=13.08$ (μm $s^{-0.31}$)
Al-0.63Mg-1.377Si [41]	—	—	0.08-0.29	$\lambda_{2C}=k_{15}t_f^{0.33}$	$k_{15}=11.81$ (μm $s^{-0.33}$)
Al-1.24Mg-0.45Si [41]	—	—	0.08-0.29	$\lambda_{2C}=k_{16}t_f^{0.26}$	$k_{16}=21.53$ (μm $s^{-0.26}$)
Al-1.55Mg-0.374Si [41]	—	—	0.08-0.29	$\lambda_{2C}=k_{17}t_f^{0.35}$	$k_{17}=11.17$ (μm $s^{-0.35}$)
A357 alloy [42]	—	—	0.3-12.8	$\lambda_{2C}=k_{18}t_f^{0.30}$	$k_{18}=20.80$ (μm $s^{-0.30}$)
Al-4.5Si-1Cu-0.5Fe [43]	—	—	0.4-6	$\lambda_{2C}=k_{19}t_f^{0.39}$	$k_{19}=7.94$ (μm $s^{-0.39}$)
Al-4.5Si-4Cu-0.5Fe [43]	—	—	0.4-10	$\lambda_{2C}=k_{20}t_f^{0.35}$	$k_{20}=7.63$ (μm $s^{-0.35}$)
Al-9Si-4Cu-0.5Fe [43]	—	—	0.2-1.8	$\lambda_{2C}=k_{21}t_f^{0.40}$	$k_{21}=4.98$ (μm $s^{-0.40}$)
Al-7Si-0.3Mg-0.15Fe [44]	—	—	0.19-6.25	$\lambda_{2C}=k_{22}t_f^{0.33}$	$k_{22}=13.30$ (μm $s^{-0.33}$)

* k value obtained by estimating on the graph

** Cooling rate, V and G values obtained by estimating on the graph

*** as-cast

on the alloy components, the composition of these components, solute diffusion and thermal diffusion caused by fluid flow. This *k* value is a constant that indicates whether SDAS is greater or lesser. The larger the experimental *k* value, the larger the SDAS value is expected to be.

3.3. Solute and phase distribution in the coarsening process

Due to the different widths of secondary dendritic arms during the growth process, the composition nearby the dendritic surface varies from place to place, and diffuses from the high solubility area (coarse secondary dendritic arms area) to the low-solubility area (fine secondary dendritic arms area), resulting in dissolution of the fine dendritic arms and coarsening of coarse dendritic arms. This situation is confirmed by Liao et al. [45]. Dendrite coarsening involves the elimination of small dendritic arms and the simultaneous growth of larger dendritic arms located in close proximity to the smaller ones. This phenomenon causes an increase of the length scale of the microstructure with increasing time [46,47]. When the growth rate increases, there is not enough time for this process, thus refining SDAS [45]. As can be seen from our experimental data in Fig. 3, the largest SDAS at low growth rate (8.3 μm/s) was about 60 mm, while the largest SDAS at high growth rate (83.0 μm/s) was 25 mm. A 58% reduction in SDAS is observed by increasing the growth rate from 8.3 to 83.0 μm/s.

Tang et al.[48] observed about 58% reduction in SDAS using a cooling rate in the range of about 2.3-24.1 K/s for the Al-5.0Mg-3.0Zn-1.0Cu alloy. This determination coincides with our results. Thus, since more time is required at low

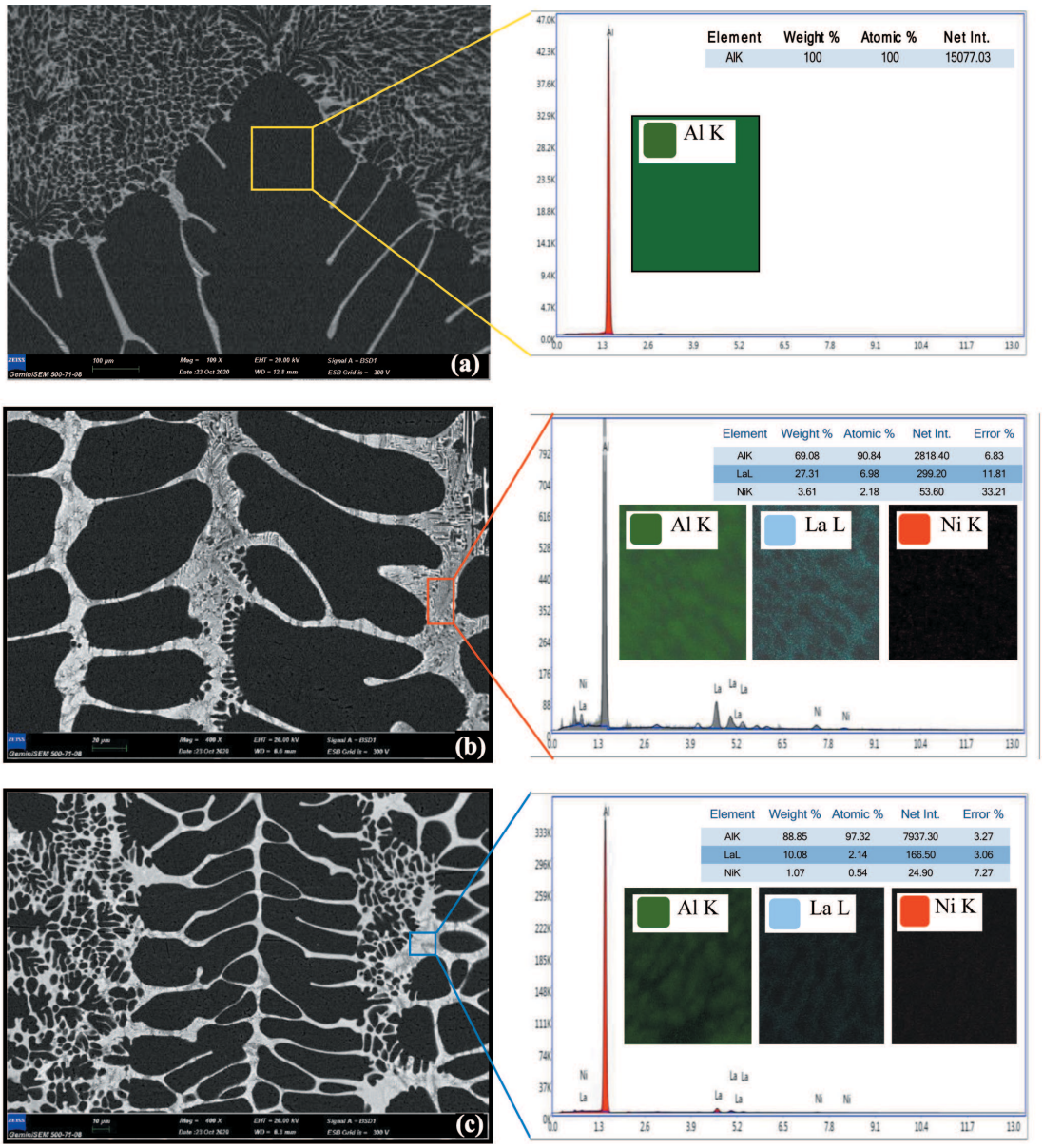

Fig. 4. EDS/elemental mapping images showing the distribution of chemical elements in the phases formed in the Al-8.8La-1.2Ni alloy sample; (a) dendrite tip growing at low growth rate (8.3 μm/s), (b) secondary dendrite arms growing at low growth rate (8.3 μm/s), (c) secondary dendrite arms growing at high growth rate (8.3 μm/s)

growth rate, the region between dendrites enriched in terms of La and Ni. This situation is apparent in the energy dispersive spectroscopy (EDS)/mapping analysis in Fig. 4. As seen from Fig. 4a, the dark area (yellow square) selected on the dendrite tip is completely the a-Al phase. While the amounts of La and Ni were 27.31 wt.% and 3.61 wt.% in specimen which solidified at low growth rate (8.3 mm/s) (Fig. 4b, red rectangle), it was determined as 10.08 wt.% and 1.07 wt.% in the specimen which solidified at high growth rate (83 mm/s) (Fig. 4c, blue square). These values obtained for the specimen solidifying at high growth rate are very close to the nominal composition of the studied alloy (Al-8.8La-1.2Ni). Thus, there was not enough time for solute microsegregation to occur. As well as the presence of α-Al dendritic phase, for the sample that solidified at low growth rate, $Al_{11}La_3$ and Al_3Ni intermetallics were observed in the inter dendritic region. This situation has been reported in a previous study by the same authors [26]. In the mentioned study [26], both EDX analysis and XRD pattern strongly indicate that only three phases (α-Al, $Al_{11}La_3$ and Al_3Ni) are present in the microstructure of the cast sample. These IMC phases show an almost homogeneous distribution in the interdendritic region. One interesting feature is that the mixed $Al/Al_{11}La_3$ and Al/Al_3Ni eutectics found interdendritically as the last regions to freeze in studied alloy do not seem to exhibit the close coupling between the $Al_{11}La_3$ and Al_3Ni phases that prevails in the fully eutectic microstructures. A possible explanation is that the prior formation of a primary phase nucleates one of the binary eutectics prior to the other one. $Al-Al_3Ni$ would probably nucleate first because its eutectic temperature (640°C) appears to be higher than that for $Al-Al_{11}La_3$ (636°C) [36].

In the mapping analysis given in the spectrum on the right part of the same figure, the distribution of each Al, La and Ni elements within the measurement regions was obtained with different colors. The variation of La and Ni solute distributions in the region between dendrites in low and high growth rate solidified specimens was also supported by mapping analysis.

Similar behaviors were reported in a study by Ferreira et al [32] for Al-3Cu-0.5Mg alloy, and this confirms our experimental results. The coarsening behavior affects the distribution of length scales, microsegregation and other microstructural characteristics of the materials, all of which determine the physical and chemical properties of the materials in terms of microhardness, tensile strength, ductility, electrical conductivity and corrosion resistance [49]. Therefore, a complete understanding of the coarsening process would improve the selection of process parameters such as G, V and C_o (composition) and the overall control of the final microstructures.

4. Conclusions

In this study, the effect of growth rate on the coarsening of the secondary dendrite arm spacing was investigated in the directionally solidified ternary Al-8.8La-1.2Ni alloy. The control of studied alloy microstructures, by manipulating directional solidification processing variables such as the cooling rate and the growth rate can be used as an alternative way to design desired properties. The main findings of the study are summarized below:

1. The mechanism III (arm fragmentation) among the existing coarsening mechanisms played an important role in the coarsening process in this study. In this coarsening mechanism, a neck was formed at the root of some second arms and continued until this arm separated from the dendrite trunk and gradually became spherical with increasing time (1-2 minutes).
2. The secondary dendritic arm spacing is very sensitive to growth rate and an increase of growth rate from 8.3 to 83 μm/s decreases SDAS from 60 to 25 μm.
3. It was also determined that t_f values decreased for increasing V values. While the growth rate increased from 8.3 to 83 μm/s, the local solidification time value for the coarsest λ_2 values decreased from 82 to 7s.
4. Experimental relationships between λ_{2C} and t_f were obtained as $\lambda_{2C} = 11.38\, t_f^{0.37}$, $\lambda_{2C} = 8.97\, t_f^{0.43}$, $\lambda_{2C} = 9.41\, t_f^{0.46}$, and $\lambda_{2C} = 9.77\, t_f^{0.47}$ for each growth rates (8.3, 16.6, 41.5 and 83.0 mm/s, respectively. These experimental relationships obtained can be used at industrial scales.
5. The exponential values (0.37, 0.43, 0.46 and 0.47) obtained by us are good agreement with the 0.33 exponential value proposed by the R-B model and the range of exponential values (0.33-0.47) obtained by other researchers.

REFERENCES

[1] M.C. Flemings, Mater. Trans. A. **46** (5), 895-900 (2005).
[2] Y. Sun, W.B. Andrews, K. Thornton, P.W. Voorhees, Sci. Rep. **8** (1), 17940 (2018).
[3] D. Kammer, P.W. Voorhees, Acta Mater. **54** (6), 1549-1558 (2006).
[4] S.P. Marsh, M.E. Glicksman, Metall. Trans. A. **27** (3), 557-567 (1996).
[5] H. Neumann-Heyme, N. Shevchenko, Z. Lei, K. Eckert, O. Keplinger, J. Grenzer, C. Beckermann, S. Eckert, Acta Mater. **146**, 176-186 (2018).
[6] T. Cool, P.W. Voorhees, Acta Mater. **127**, 359-367 (2017).
[7] J.L. Fife, P.W. Voorhees, Acta Mater. **57** (8), 2418-2428 (2009).
[8] S. Terzi, L. Salvo, M. Suery, A.K. Dahle, E. Boller, Acta Mater. **58** (1), 20-30 (2010).
[9] N.L.M. Veldman, A.K. Dahle, D.H. Stjohn, L. Arnberg, Metall. Trans. A. **32**, 147-155 (2001).
[10] L. Collini, G. Nicoletto, R. Konecna, Mater. Sci. Eng. A. **488** (1-2), 529-539 (2008).
[11] K.P. Young, D.H. Kirkwood, Metall. Trans. A. **6**, 197-205 (1975).
[12] B. Li, Ph.D. Thesis, University of Connecticut, Connecticut (2004).
[13] T.Z. Kattamis, J.C. Coughlin, M.C. Flemings, T. Metall. Soc. AIME **239**, 1504-1511 (1967).
[14] M.C. Flemings, D.R. Poirier, R.V. Barone, H.D. Brody, JISI Lond. **208**, 371-381 (1970).
[15] M.C. Flemings, Metall. Trans. B. **5**, 2121-2134 (1974).

[16] U. Feurer, R. Wunderlin, Fachbericht der Deutschen Gesellschaft für Metallkunde, Oberursel, FRG, 1977.
[17] K.J. Oswald, M.S. Misra, AFS Trans. **88**, 845-862 (1980).
[18] A. Inoue, M. Kohinata, A. Tsai, T. Masumoto, Mat. Trans. JIM **30** (5), 378-381 (1989).
[19] P. Dantzer, J. Less-Common Met. **131** (1-2), 349-363 (1987).
[20] H. Feufel, F. Schuller, J. Schmid, F. Sommer, J. Alloys and Compds. **267**, 234-244 (1997).
[21] P.P. Choi, J.S. Kim, O.T.H. Nguyen, D.H. Kwon, Y.S. Kwon, J.C. Kim, Mater. Sci. Eng. A. **449-451**, 1119-1122 (2007).
[22] M. Rappaz, W.J. Boettinger, Acta Mater. **47** (11), 3205-3219 (1999).
[23] H.-J. Diepers, C. Beckermann, I. Steinbach, Acta Mater. **47** (13), 3663-3678 (1999).
[24] S. Steinbach, L. Ratke, Mat. Sci. Eng. A. **413-414**, 200-204 (2005).
[25] M. Easton, C. Davidson, D. St John, Metall. Trans. A **41** (6), 1528-1538 (2010).
[26] E. Üstün, E. Çadırlı, J. Alloys and Compds. **855**, 157331 (2021).
[27] M. Jaradeh, T. Carlberg, Mat. Sci. Technol. **23** (4), 475-482 (2007).
[28] M. Kahlweit, Scripta Metall. **2** (5), 251-254 (1968).
[29] M.C. Flemings, T.Z. Kattamis, B.P. Bardes, AFS Trans. **176**, 501-506 (1991).
[30] M. Tiryakioğlu, Metall. Trans. A. **50**, 3030-3032 (2019).
[31] A. F. Ferreira, J.A. Castroa, L.O. Ferreira, Materials Research **20** (1), 68-75 (2016).
[32] I.L. Ferreira, A.L.S. Moreira, J.A.S. Aviz, T.A. Costa, O.L. Rocha, A.S. Barros, A. Garcia, J. Manuf. Process. **35**, 634-650 (2018).
[33] M. Chen, T.Z. Kattamis, Mater. Sci. Eng. A. **247** (1-2), 239-247 (1998).
[34] B. Donadoni, G.L. Gouveia, A. Garcia, J.E. Spinelli, J. Manuf. Process. **54**, 14-18 (2020).
[35] P.A.D. Jacome, M.C. Landim, A. Garcia, A.F. Furtado, I.L. Ferreira, Thermochim. Acta **523** (1-2), 142-149 (2011).
[36] A. Juarez-Hernandez, H. Jones, J. Cryst. Growth **208** (1-4), 442-448 (2000).
[37] G. Matache, D. M. Stefanescu, C. Puscasu, E. Alexandrescu, Int. J. Cast Metal. Res. **29** (5), 303-316 (2016).
[38] G. Matache, D. M. Stefanescu, C. Puscasu, E. Alexandrescu, A. Bührig-Polaczek, Int. J. Cast Metal. Res. **28** (6), 323-336 (2015).
[39] Q. S. Hamed, R. Elliott, Cast Metals **6** (1), 36-41 (1993).
[40] V. Ronto, A. Roosz, Int. J. Cast Metal. Res. **13** (6), 337-342 (2001).
[41] V. Ronto, A. Roosz, Int. J. Cast Metal. Res. **14** (2), 131-135 (2001).
[42] J. He, J.M. Zeng, A. Yan, Adv. Mater. Res. **51**, 8-92 (2008).
[43] T. Sivarupan, C.H. Caceres, J.A. Taylor, Metall. Trans. A **44** (9), 4071-4080 (2013).
[44] R. Chen, Y.F. Shi, Q.Y. Xu, B.C. Liu, Trans. Nonferrous Met. Soc. China **24** (6), 1645-1652 (2014).
[45] H. Liao, Y. Sun, G. Sun, Mater. Sci. Eng. A. **335** (1-2), 62-66 (2002).
[46] J.A. Dantzig, M. Rappaz, Solidification, EPFL Press, Lausanne, Switzerland (2009).
[47] V. Fourlakidis, A. Dioszegi, Mater. Sci. Eng. A. **618**, 161-167 (2014)
[48] H.P. Tang, Q.D. Wang, C. Lei, B. Ye, K. Wang, H.Y. Jiang, W.J. Ding, X.F. Zhang, Z. Lin, J.B. Zhang, J. Alloys and Compds. **801**, 596-608 (2019).
[49] J. Wang, G. Yang, Acta Mater. **56** (17), 4585-4592 (2008).